



# Size- and position-controlled Ge nanocrystals separated by high-*k* dielectrics

D. Lehninger, F. Honeit,\*<sup>1</sup> D. Rafaja, V. Klemm, C. Röder, L. Khomenkova,<sup>2</sup> F. Schneider, J. von Borany, and J. Heitmann

## Impact statement

The use of germanium nanocrystals for applications, such as floating gate memory cells, is very difficult due to challenges in size and position control. This article presents important steps toward the solution of those challenges in the material system germanium/tantalumzirconiumoxide. Our path allows the formation of electrically isolated nanocrystals between 3 and 6 nm in diameter embedded in an amorphous high-*k* matrix. In comparison to our previous publication, which mentioned the general possibility of size-controlled germanium nanocrystals in tantalumzirconiumoxide, details and limits of this material system and the influence of an additional SiO<sub>2</sub> interlayer are shown here.

Germanium nanocrystals embedded in high-*k* dielectric matrices are of main interest for infrared sensing application, as a role model for Ge-based nanoelectronics passivation or for nonvolatile memory devices. The capability of the size control of those nanocrystals via rapid thermal processing of superlattice structures is shown for the [Ge–TaZrO<sub>*x*</sub>/TaZrO<sub>*x*</sub>]<sub>*n*</sub>, [Ge–TaZrO<sub>*x*</sub>/SiO<sub>2</sub>/TaZrO<sub>*x*</sub>]<sub>*6*</sub>, and [TaZrO<sub>*x*</sub>/Ge–SiO<sub>2</sub>]<sub>*n*</sub> superlattice systems. All superlattices were deposited by radiofrequency magnetron sputtering. Transmission electron microscopy (TEM) imaging confirms the formation of spherically shaped nanocrystals. Raman scattering proved the crystallization of Ge above 700°C. The TaZrO<sub>*x*</sub> crystallizes above 770°C, associated with a phase separation of Ta<sub>2</sub>O<sub>5</sub> and ZrO<sub>2</sub> as confirmed by x-ray diffraction. For the composite layers having 3 nm and 6 nm thickness, the size of the Ge nanocrystals correlates with the deposited layer thickness. Thicker composite layers (above 9 nm) form two fractions of nanocrystals with different sizes. An additional SiO<sub>2</sub> layer in the [Ge–TaZrO<sub>*x*</sub>/SiO<sub>2</sub>/TaZrO<sub>*x*</sub>]<sub>*6*</sub> superlattice stacks facilitates the formation of larger and better separated Ge nanocrystals. The deposition of Ge–SiO<sub>2</sub> composite layers separated by pure TaZrO<sub>*x*</sub> illustrates the barrier effect of TaZrO<sub>*x*</sub> against Ge diffusion. All three material systems allow the controlled formation of Ge nanocrystals in amorphous matrices at temperatures above 700 and below 770°C.

## Introduction

Semiconductor nanocrystals embedded in dielectric matrices have been widely studied over the last decades. In particular, Si and Ge nanocrystals are considered for applications as absorbers for the third generation of solar cells,<sup>1</sup> as sensitizers enhancing the luminescence of rare earth elements,<sup>2, 3</sup> as light emitters<sup>4</sup> for integrated photonics, and as charge storage nodes for nanocrystal-based nonvolatile memory devices.<sup>5, 6</sup>

Ge nanocrystals are compatible with current CMOS technologies and offer benefits compared to Si nanocrystals such as a lower crystallization temperature and larger exciton Bohr radius. The synthesis of Ge nanocrystals can be realized by Ge ion implantation into an oxide matrix<sup>7</sup> or by deposition of Ge-rich oxide films using chemical vapor deposition (CVD),<sup>8</sup> sputtering techniques,<sup>9</sup> or evaporation<sup>10</sup> followed by thermally triggered phase

D. Lehninger, Institute of Applied Physics, TU Bergakademie Freiberg, Freiberg, Germany

F. Honeit, Institute of Applied Physics, TU Bergakademie Freiberg, Freiberg, Germany; Florian.Honeit@physik.tu-freiberg.de

D. Rafaja, Institute of Materials Science, TU Bergakademie Freiberg, Freiberg, Germany

V. Klemm, Institute of Materials Science, TU Bergakademie Freiberg, Freiberg, Germany

C. Röder, Institute of Applied Physics, TU Bergakademie Freiberg, Freiberg, Germany; Institute of Theoretical Physics, TU Bergakademie Freiberg, Freiberg, Germany

L. Khomenkova, V. Lashkaryov Institute of Semiconductor Physics, Kyiv, Ukraine; National University of "Kyiv-Mohyla Academy," Kyiv, Ukraine

F. Schneider, Institute of Applied Physics, TU Bergakademie Freiberg, Freiberg, Germany

J. von Borany, Institute of Ion Beam Physics and Materials Research, Helmholtz-Zentrum Dresden-Rossendorf, Dresden, Germany

J. Heitmann, Institute of Applied Physics, TU Bergakademie Freiberg, Freiberg, Germany

\*Corresponding author

doi:10.1557/s43577-022-00311-8



separation and Ostwald ripening of Ge clusters and their crystallization. The size control is normally realized by adjusting the Ge content in the oxide matrix<sup>11</sup> or using tailored annealing temperatures<sup>12–14</sup> or annealing times.<sup>15</sup> However, the broad size distributions resulting from these methods may deteriorate the electronic and optical properties of the final devices.

A more promising way to prepare nanocrystals of controlled size, position, and areal density is a high-temperature treatment of superlattice structures. When annealing alternating composite (semiconductor and matrix material) and pure (matrix material only) layer stacks, the interplay between Gibbs energy and interface energy restricts the formation of the semiconductor nanocrystals to roughly the thickness of the mixed layers.

This approach was initially applied to obtain Si nanocrystals in a SiO<sub>2</sub> matrix.<sup>16, 17</sup> For Ge, this approach was documented by Zschintzsch et al.,<sup>18</sup> who used a periodic arrangement of thin Ge-rich GeO<sub>x</sub> layers separated by SiO<sub>2</sub> layers. In the case of this approach, the prevention of Ge diffusion into the separation layer is one important requirement. Therefore, the choice of the separation layer material is crucial. Only if the material is a good barrier against the Ge diffusion, the position and size of the Ge nanocrystals can be controlled by the location of the Ge-rich layers and by its thicknesses, respectively. Furthermore, the thickness of the separation layers determines the distances between the layers containing Ge nanocrystals and hence the nanocrystal density across the stack.<sup>19</sup> There are several studies about embedding Ge nanocrystals in different matrix materials like AlO<sub>x</sub>,<sup>20, 21</sup> SiC,<sup>22</sup> or GeO<sub>x</sub>.<sup>23</sup>

In this study, ZrO<sub>2</sub>-based matrix materials are used. ZrO<sub>2</sub> shows good barrier properties against Ge diffusion,<sup>24</sup> and possesses a high bandgap of 5.1–7.1 eV<sup>25, 26</sup> as well as a high permittivity of 20–47 depending on its crystal structure.<sup>27</sup> Because of the marginal miscibility of ZrO<sub>2</sub> and Ge, the growth of Ge nanocrystals within a ZrO<sub>2</sub> matrix is possible via phase segregation of Ge from Ge-rich Ge-ZrO<sub>x</sub> layers separated by ZrO<sub>2</sub> layers. Attempts have been made to use [Ge-ZrO<sub>x</sub>/ZrO<sub>2</sub>] superlattices for controlled formation of Ge nanocrystals within a ZrO<sub>2</sub> matrix.<sup>28–30</sup> However, this approach has two drawbacks. It leads to the formation of elongated Ge clusters with insufficiently controlled size, shape and spatial distribution.<sup>28</sup> Furthermore, the crystallization of Ge and ZrO<sub>2</sub> occurs simultaneously at about 660°C.<sup>9, 24</sup>

Amorphous matrices provide potentially better passivation of the nanocrystal surface, which is required to observe quantum confinement effects by preventing the instant recombination of an exciton<sup>31</sup> and can suppress leakage currents through the stack more efficiently (due to the absence of grain boundaries). The latter effect helps to suppress discharging of the nanocrystals across the blocking oxide, if the Ge nanocrystals are used in nonvolatile memories.<sup>32</sup>

Recently, it has been shown that the crystallization temperature of ZrO<sub>2</sub> can be increased by adding tantalum into

the ZrO<sub>2</sub> layers.<sup>33</sup> Based on this result, the work presented here discusses the use of TaZrO<sub>x</sub> as separation layers in [Ge–TaZrO<sub>x</sub>/TaZrO<sub>x</sub>]<sub>n</sub> superlattices for controlled formation of Ge nanocrystals within an amorphous high-*k* matrix. For this purpose, [Ge–TaZrO<sub>x</sub>/TaZrO<sub>x</sub>]<sub>n</sub> superlattices with different thicknesses of the periodic motif were deposited and subjected to a rapid thermal annealing process. Furthermore, the effect of additional SiO<sub>2</sub> separation layers on the formation of Ge nanocrystals in [Ge–TaZrO<sub>x</sub>/SiO<sub>2</sub>/TaZrO<sub>x</sub>]<sub>6</sub> superlattice stacks was studied. For comparison, the formation of separated Ge nanocrystals with controlled size in [Ge–SiO<sub>2</sub>/TaZrO<sub>x</sub>] superlattice structures was investigated as well.

## Experimental

The [Ge–TaZrO<sub>x</sub>/TaZrO<sub>x</sub>]<sub>10</sub>, [Ge–TaZrO<sub>x</sub>/SiO<sub>2</sub>/TaZrO<sub>x</sub>]<sub>6</sub>, and [TaZrO<sub>x</sub>/Ge–SiO<sub>2</sub>]<sub>n</sub> stacks were fabricated using an rf magnetron sputtering system, equipped with three plasma sources carrying 3" Ge, ZrO<sub>2</sub>/Ta<sub>2</sub>O<sub>5</sub> and SiO<sub>2</sub> targets, respectively. In the sputtering chamber, the targets are arranged confocally in a top-down approach above the substrate, which is rotated during the deposition. The sputtering processes were performed by an argon plasma, without substrate heating, at a pressure of 5.2·10<sup>–3</sup> mbar. The applied power densities, used for the deposition of the respective layer, are given in **Table I**. As substrates, <100> silicon wafers were used, which were subjected to a standard RCA cleaning procedure, dipped in diluted hydrofluoric acid, and immediately transferred to an oxidation chamber to form a 3-nm-thin SiO<sub>2</sub> layer by dry oxidation. The Ge–TaZrO<sub>x</sub> composite layers were co-sputtered using a confocal arrangement of a Ge target and a mixed ZrO<sub>2</sub>/Ta<sub>2</sub>O<sub>5</sub> target with a Ta content of 17 at.%. Pure TaZrO<sub>x</sub> and pure SiO<sub>2</sub> layers were deposited by sputtering only the ZrO<sub>2</sub>/Ta<sub>2</sub>O<sub>5</sub> or the SiO<sub>2</sub> target, respectively. To avoid the evaporation of volatile GeO and the oxidation of Ge in the layers during annealing, all stacks were covered by a top 10-nm SiO<sub>2</sub> capping layer.

Four different superlattice structures were deposited. Superlattice SL1 is a [Ge–TaZrO<sub>x</sub>/TaZrO<sub>x</sub>]<sub>10</sub> stack consisting of 10 periods of alternating Ge–TaZrO<sub>x</sub> composite and pure TaZrO<sub>x</sub> separation layers with a thickness of 5 nm each. In order to reveal the influence of the Ge–TaZrO<sub>x</sub> composite layer thickness on the nanocrystal size, a [Ge–TaZrO<sub>x</sub>/TaZrO<sub>x</sub>]<sub>14</sub> stack with four composite layers of varied thickness between 3 and 12 nm and a constant Ge concentration was fabricated (SL2). To show the influence of a SiO<sub>2</sub> layer on the phase separation and nucleation processes, a [SiO<sub>2</sub>/Ge–TaZrO<sub>x</sub>/TaZrO<sub>x</sub>]<sub>6</sub> stack was fabricated (SL3), comprising an additional SiO<sub>2</sub> interlayer beneath each composite layer. For comparison a [Ge–SiO<sub>2</sub>/TaZrO<sub>x</sub>]<sub>9</sub> superlattice was sputtered (SL4). The detailed sputtering conditions are given in **Table I**.

The chemical composition of the as-deposited films (SL1, SL2, and SL3) was determined by Rutherford backscattering spectrometry (RBS) using helium ions with an energy of


**Table 1. RF sputter deposition parameters of the investigated superlattice structures.**

SL#	Composite Layer			Separation Layer			Interlayer		
	Material	RF Power Density (W/cm <sup>2</sup> )	Thickness (nm)	Material	RF Power Density (W/cm <sup>2</sup> )	Thickness (nm)	Material	RF Power Density (W/cm <sup>2</sup> )	Thickness (nm)
SL1	Ge	1.3	5	TaZrO <sub>x</sub>	3.3	5	–	–	–
	TaZrO <sub>x</sub>	3.3							
SL2	Ge	2.2	3, 6, 9, 12	TaZrO <sub>x</sub>	3.3	7	–	–	–
	TaZrO <sub>x</sub>	3.3							
SL3	Ge	2.2	3, 6, 9, 12, 15, 25	TaZrO <sub>x</sub>	3.3	7	SiO <sub>2</sub>	3.3	5
	TaZrO <sub>x</sub>	3.3							
SL4	Ge	1.87	3	TaZrO <sub>x</sub>	3.3	6	–	–	–
	SiO <sub>2</sub>	3.3							

1.7 MeV (normal incidence, scattering angle 170°). For the RBS experiments, single composite films were deposited on glassy carbon substrates (to enable a background-free oxygen signal) using the same deposition conditions as previously stated. According to RBS, the Ge-rich layers contained 19 at.% Ge, 12 at.% Ta, 9 at.% Zr, and 60 at.% O in the case of SL1 and 36 at.% Ge, 9 at.% Ta, 7 at.% Zr, and 48 at.% O in the case of SL2 and SL3. The chemical composition of the separation layers is always 17 at.% Ta, 12 at.% Zr, and 71 at.% of O. The relative uncertainties of about 5% for the heavy elements Ge, Zr, and Si with well-known cross sections are smaller than the relative uncertainty for O (about 10%).

To trigger the segregation and crystallization processes, the multilayer stacks were annealed for 30 s at temperatures between 650°C and 800°C in a nitrogen atmosphere using a rapid thermal processing (RTP) tool.

The size, form, and spatial distribution of the Ge nanoclusters were analyzed on cross-section specimens using a JEOL 2200 FS transmission electron microscope (TEM), which is equipped with a corrector for spherical aberration in the illumination system. In order to enhance the visibility of the nanoclusters, the Fresnel defocus mode was employed, which can lead to an overestimation of the crystallite size.

Raman scattering and glancing angle x-ray diffraction (GAXRD) measurements were performed to study the crystallization temperatures of individual phases in this system. All Raman spectra were detected in the 50–600 cm<sup>-1</sup> spectral range using a LabRAM HR 800 spectrometer (Horiba Jobin Yvon) with a thermoelectrically cooled CCD detector. The spectrometer was equipped with gratings of 1800 grooves/mm. Raman scattering was excited by a 532-nm (2.33 eV) spectral line of a frequency-doubled Nd:YAG laser. The linearly polarized laser beam was focused on the sample surface using a 100× Olympus microscope objective (numerical aperture 0.80) with a long working distance. In order to avoid laser-induced heating or thermal decomposition of the samples, the applied laser power was adjusted by a filter and kept very low (0.4–0.5 mW).

The GAXRD patterns were measured with a thin-film diffractometer (X'Pert from PANalytical), which was equipped with a 0.4° equatorial Soller collimator and with a planar Ge monochromator, both located in the diffracted beam. CuK<sub>α</sub> radiation ( $\lambda_1=0.15406$  nm and  $\lambda_2=0.15444$  nm) was used. The GAXRD patterns were collected in a 2 $\theta$  range between 10° and 90° at a fixed glancing angle of incidence of 1°. The small incidence angle reduces the penetration depth of x-rays into the sample and increases the scattering power of the thin films. In order to avoid the substrate reflection 311, all samples were mounted with a 45° rotation between the [001] direction of the (100)-oriented Si wafer and the diffraction plane. The instrumental broadening of the diffractometer was determined using a LaB<sub>6</sub> standard from NIST. To interpret the GAXRD pattern Rietveld analysis, performed with the MAUD software were used.<sup>34, 35</sup>

## Results and discussion

### Formation of Ge nanocrystals in Ge-TaZrO<sub>x</sub>/TaZrO<sub>x</sub> superlattices [SL1]

Rapid thermal annealing triggers the segregation of Ge from originally intermixed continuous Ge-TaZrO<sub>x</sub> layers and stimulates the desired nucleation, growth, and crystallization of Ge nanoclusters, but also the undesirable crystallization of the TaZrO<sub>x</sub> matrix. Therefore, the temperature of the rapid thermal annealing must be adjusted between the crystallization temperatures of Ge and TaZrO<sub>x</sub>.

The crystallization temperature of the Ge nanoparticles was determined using Raman spectroscopy on the superlattice stack SL1, having 19 at.% Ge in the Ge-rich layers. Individual samples were annealed at temperatures between 650°C and 800°C (**Figure 1**). The Raman spectra of the as-deposited sample and the sample annealed at 650°C show a broad band at about 275 cm<sup>-1</sup>, which is a feature of the amorphous contributions of Ge and matrix.<sup>24</sup> The weak signal at around 300 cm<sup>-1</sup> is the second order transverse acoustic (2TA) phonon mode of the silicon substrate.<sup>36</sup> The transition from amorphous Ge (or from Ge dissolved in

Ge–TaZrO<sub>x</sub>) to crystalline Ge is observable between 650°C and 700°C, as indicated by the steep increase of the intensity of the signal at about 300 cm<sup>-1</sup>, which belongs to the  $\Gamma_{25'}$  optical phonon at the  $\Gamma$ -point in the Brillouin-zone.<sup>37</sup> Annealing at higher temperatures further reduces the full width at half maximum of the phonon mode and leads to a more symmetric shape of this mode. This indicates a continuous improvement of the grade of crystallinity in the Ge clusters.

The crystallization temperature of the amorphous TaZrO<sub>x</sub> matrix was determined using glancing angle x-ray diffraction. **Figure 2** depicts GAXRD patterns of superlattice SL1 annealed at 750°C, 770°C, and 800°C. The sample annealed at 750°C revealed three broad reflections at  $2\theta \approx 27^\circ$ ,  $2\theta \approx 45^\circ$ , and  $2\theta \approx 55^\circ$ , which originate from nanocrystalline Ge, and two broad peaks at  $2\theta \approx 30^\circ$  and  $2\theta \approx 52^\circ$  that can be attributed to the amorphous matrix. The crystallization of the matrix starts at 770°C annealing temperature, demonstrated by the sharp reflection at  $2\theta \approx 30^\circ$  originated by an orthorhombic phase of TaZrO<sub>x</sub>.<sup>33</sup> According to the Raman measurement (Figure 1), the temperature window to synthesize Ge nanocrystals within an amorphous matrix is thus between 700°C and 770°C. After annealing at 800°C, three crystalline phases were identified in the sample: cubic Ge with the space group  $Fd\bar{3}m$ , orthorhombic (Zr,Ta)O<sub>2</sub> with the space group  $Pbc2_1$ , and orthorhombic (Ta,Zr)<sub>2</sub>O<sub>5</sub> with the space group  $C2mm$ .<sup>33</sup>

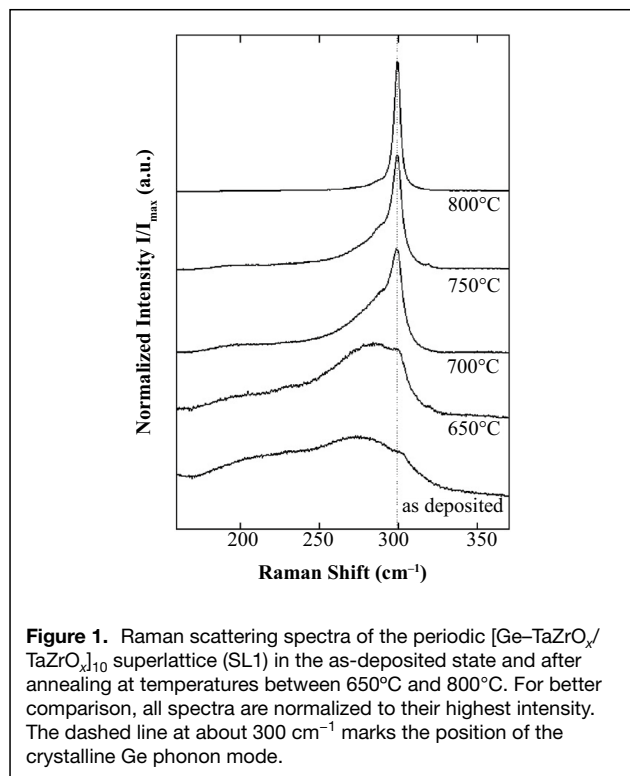


**Figure 1.** Raman scattering spectra of the periodic [Ge–TaZrO<sub>x</sub>/TaZrO<sub>x</sub>]<sub>10</sub> superlattice (SL1) in the as-deposited state and after annealing at temperatures between 650°C and 800°C. For better comparison, all spectra are normalized to their highest intensity. The dashed line at about 300 cm<sup>-1</sup> marks the position of the crystalline Ge phonon mode.

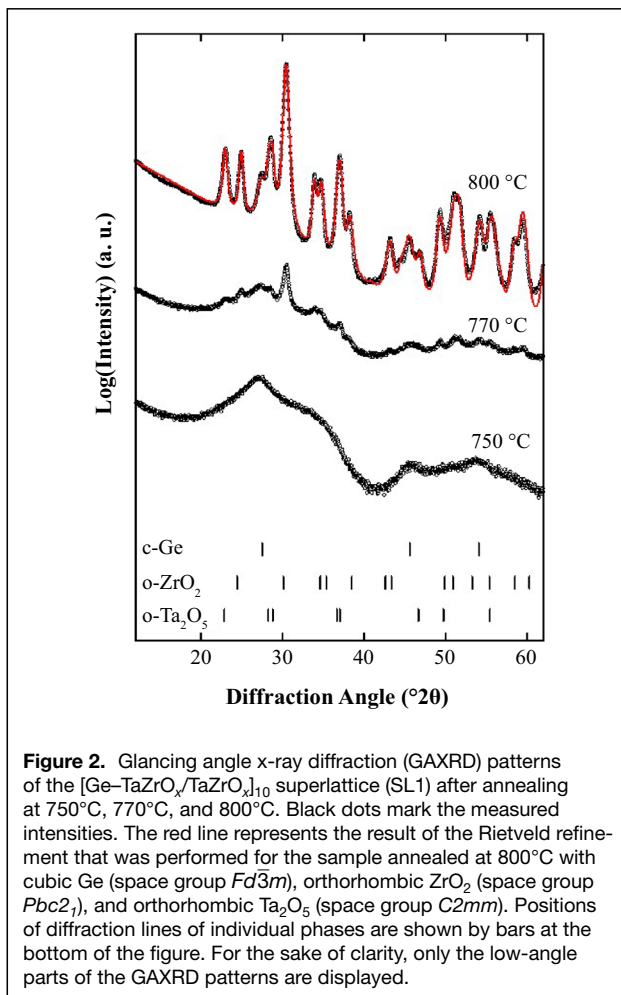


**Figure 2.** Glancing angle x-ray diffraction (GAXRD) patterns of the [Ge–TaZrO<sub>x</sub>/TaZrO<sub>x</sub>]<sub>10</sub> superlattice (SL1) after annealing at 750°C, 770°C, and 800°C. Black dots mark the measured intensities. The red line represents the result of the Rietveld refinement that was performed for the sample annealed at 800°C with cubic Ge (space group  $Fd\bar{3}m$ ), orthorhombic ZrO<sub>2</sub> (space group  $Pbc2_1$ ), and orthorhombic Ta<sub>2</sub>O<sub>5</sub> (space group  $C2mm$ ). Positions of diffraction lines of individual phases are shown by bars at the bottom of the figure. For the sake of clarity, only the low-angle parts of the GAXRD patterns are displayed.

The presence of Ge nanocrystals in the annealed Ge–TaZrO<sub>x</sub>/TaZrO<sub>x</sub> multilayers (SL1) was confirmed by HRTEM (**Figure 3**). The formation of Ge nanoclusters is triggered by the interplay between the Gibbs energy of the metastable Ge–TaZrO<sub>x</sub> solid solution and the interface energy of the Ge/TaZrO<sub>x</sub> interfaces. A horizontal arrangement of the nanocrystals is supported by the presence of TaZrO<sub>x</sub> separation layers. The volume density of Ge nanocrystals depends on the Ge concentration and thickness of the Ge–TaZrO<sub>x</sub> layers, and on the Ge–TaZrO<sub>x</sub>/TaZrO<sub>x</sub> thickness ratio.

Rietveld analysis of the GAXRD patterns of the superlattice SL1 annealed at 800°C (Figure 3) revealed crystallite sizes and lattice parameters of individual phases that are summarized in Table I. Cubic Ge was refined in the space group  $Fd\bar{3}m$ ,<sup>38</sup> orthorhombic (Zr,Ta)O<sub>2</sub> in the space group  $Pbc2_1$ ,<sup>40</sup> and orthorhombic Ta<sub>2</sub>O<sub>5</sub> in the space group  $C2mm$ .<sup>39</sup> The used TaZrO<sub>x</sub> sputtering target with the same amount of Ta and Zr leads to an interaction of both orthorhombic phases and changes the lattice parameters.<sup>6</sup> Crystallite sizes were determined using the Williamson–Hall approach.<sup>41</sup>

After annealing at 800°C, the size of the Ge nanocrystals in superlattice SL1 determined using XRD was  $(8.0 \pm 1.0)$

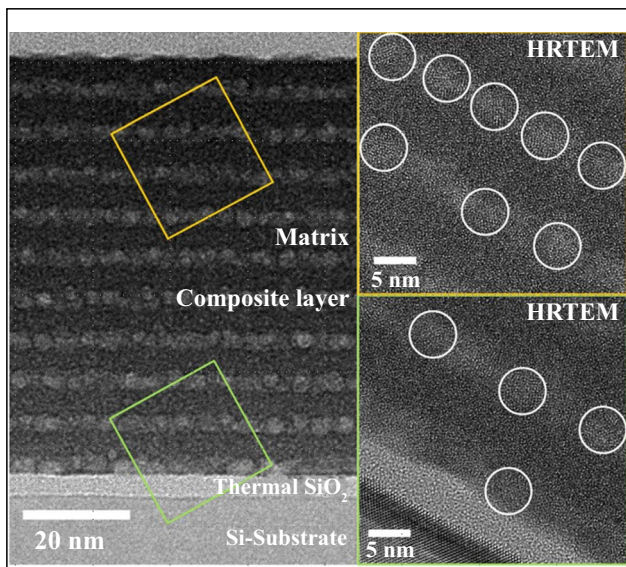


**Figure 3.** Defocused transmission electron microscope (TEM) micrographs of a  $[\text{Ge-TaZrO}_x/\text{TaZrO}_x]_{10}$  superlattice stack (SL1) after annealing at  $725^\circ\text{C}$ . The marked areas in the defocused micrograph (left) are shown in high-resolution (HRTEM) micrographs on the right-hand side of the figure in order to confirm the crystallinity of the Ge clusters and the amorphous nature of the  $\text{TaZrO}_x$  separation layers.

nm. These nanocrystals are significantly larger than the Ge nanocrystals annealed at  $725^\circ\text{C}$ , which size was  $(3.1 \pm 1.3)$  nm as revealed by the HRTEM micrograph (Figure 3). The larger size of Ge nanocrystals in the superlattice annealed at a higher temperature is a consequence of Ostwald ripening of Ge nanoclusters. However, the Ge nanocrystals in superlattice SL1 annealed at  $800^\circ\text{C}$ , determined by XRD, are even larger than the thickness of the original Ge– $\text{TaZrO}_x$  composite layers (5 nm). This phenomenon can be explained by a decreasing of the barrier effect of  $\text{TaZrO}_x$  against Ge at higher temperatures. Note that the different techniques of size determination can lead to different results, but the difference in the size is too significant to be caused by the method only. The average sizes, also identified by XRD, of the  $\text{Ta}_2\text{O}_5$

and  $(\text{Zr,Ta})\text{O}_2$  crystallites are  $(20 \pm 1)$  nm and  $(24 \pm 1)$  nm, respectively. Both sizes are also significantly larger than the original thickness of the  $\text{TaZrO}_x$  separation layers. Obviously, the crystallites of the oxide matrix grow coherently not only through the original separation layers, but also through the original Ge– $\text{TaZrO}_x$  composite layers. A similar effect was already reported for annealed Fe/Au multilayers.<sup>42</sup>

From the difference between the measured lattice parameters of Ge and  $\text{Ta}_2\text{O}_5$  and the corresponding reference values (Table II) it follows that the phase segregation (Ge,  $\text{ZrO}_2$ ,  $\text{Ta}_2\text{O}_5$ ) is not fully complete at the annealing temperature of  $800^\circ\text{C}$  and the annealing time of 30 s.  $\text{ZrO}_2$  contains Ta that acts as a stabilizer of the metastable orthorhombic crystal structure of zirconia.<sup>33</sup> Vice versa,  $\text{Ta}_2\text{O}_5$  contains possibly a small amount of Zr. From the thermodynamic point of view, Ge can accommodate less than  $4.5 \times 10^{-3}$  tantalum<sup>43</sup> and much less than  $5 \times 10^{-5}$  oxygen.<sup>44</sup> The expected maximum concentration of Zr in Ge is even lower. Presence of the impurities in the Ge nanocrystals can only be assumed from the deviation of its lattice parameter from the intrinsic value (Table II). As several foreign elements can be involved, it is not possible to determine their concentrations solely from a single lattice parameter.

The main reason for the presence of impurities in Ge is the intermixing of the elements during the deposition process. During the annealing, Ge segregates from the other elements and the Ge nanocrystals are "purified." As the out-diffusion that accompanies this process is facilitated by the temperature and time of the annealing process, a strategy to reduce the amount of impurities further is the increase of the thermal budget. Higher temperatures lead to the crystallization of the matrix material (see Table II), so that a longer annealing time might be preferable.

Pure oxygen interstitials are not problematic due to their electric inactivity.<sup>45</sup> The effects of high- $k$  cations like Zr in Ge induced by high- $k$  oxide/Ge interfaces were investigated by DFT calculations, which revealed that Zr is able to form clusters either with vacancies or with oxygen interstitials, both reducing the charge carrier mobility, which is not a relevant parameter in nanocrystals. However, the formation of high- $k$ -Ge–O clusters should occur at the Ge-matrix interface in this

**Table II.** Structure and microstructure parameters obtained from Rietveld analysis of the GAXRD patterns of superlattice SL1 annealed at  $800^\circ\text{C}$ .

Phase	Space Group	Rietveld Refinement		Literature Data
		Crystallite Size (nm)	Lattice Parameters (nm)	Lattice Parameters (nm)
Ge	$Fd\bar{3}m$	$8 \pm 1$	$a = 0.5635 \pm 0.0002$	$a = 0.5646133 \pm 0.000001^{38}$
$(\text{Ta,Zr})_2\text{O}_5$	$C2mm$	$20 \pm 1$	$a = 0.6320 \pm 0.0001$ $b = 0.35851 \pm 0.00008$ $c = 0.38866 \pm 0.00009$	$a = 0.62$ $b = 0.366$ $c = 0.389^{39}$
$(\text{Zr,Ta})\text{O}_2$	$Pbc2_1$	$24 \pm 1$	$a = 0.48709 \pm 0.00009$ $b = 0.53028 \pm 0.00009$ $c = 0.51790 \pm 0.00008$	$a = 0.48706 \pm 0.00005$ $b = 0.53065 \pm 0.00005$ $c = 0.51902 \pm 0.00005$ for $[\text{Ta}]/([\text{Ta}] + [\text{Zr}]) = 0.57^{32}$

process.<sup>45</sup> Other effects (e.g., on the optical properties) cannot be excluded, but have not yet been reported in the literature to the best of our knowledge.

### Effect of the Ge–TaZrO<sub>x</sub> layer thickness and Ge concentration on the formation of Ge nanocrystals [SL2]

The influence of the Ge–TaZrO<sub>x</sub> composite layer thickness on the phase segregation and Ge nucleation was studied with the superlattice structure SL2, which contains composite layers with a constant Ge concentration of 36 at.% and successively increasing thickness. The thickness of the separation layers was kept constant at 7 nm. As the Ge concentration in this sample series is higher than in superlattice SL1 (19 at.%), also the effect of the Ge concentration on the formation of Ge nanocrystals is illustrated by this experiment.

HRTEM micrographs of the superlattice SL2 (Figure 4) prove that the originally continuous Ge–TaZrO<sub>x</sub> layers become fragmented after annealing for 30 s at 725°C. As described for SL1, this fragmentation is driven by phase segregation and accompanied by the nucleation, growth and crystallization of Ge nanoclusters. However, the comparison with the superlattice SL1 (Figure 3) shows that a higher Ge concentration in the Ge–TaZrO<sub>x</sub> layers facilitates the formation of separated Ge nanoclusters. This phenomenon is a consequence of the concentration dependence of the Gibbs energy in immiscible or metastable systems. As the Gibbs energy of the GeTaZrO<sub>x</sub> solid solution increases with increasing Ge content (up to 50 mol% Ge), the driving force for the phase decomposition increases with increasing Ge content as well. Furthermore, a higher Ge concentration in Ge–TaZrO<sub>x</sub> leads to the formation of Ge nanoclusters with a larger volume.

The size and size distribution of the Ge nanocrystals depends strongly on the composite layer thickness (Figures 4 and 5). The quantity and the size of the nanocrystals were determined by visual inspection. Ge nanocrystals formed from the first composite layer having the thickness of 3 nm exhibit an average size of  $(4.7 \pm 0.8)$  nm (Figure 5a), which is slightly larger than the thickness of the original composite layer. Nanocrystals formed in the second layer (thickness 6 nm) have an average size of  $(6.2 \pm 1.3)$  nm (Figure 5b). In the third layer having the thickness of 9 nm, the size distribution of the Ge nanocrystals had to be fitted with a bimodal size distribution leading to average nanocrystal sizes of  $(4.4 \pm 1.5)$  nm and  $(8.2 \pm 1.6)$  nm (see Figure 5c). A bimodal size distribution was also observed for the Ge nanocrystals in the fourth composite layer having the thickness of 12 nm. The fitted average sizes of the nanocrystals are  $(5.4 \pm 1.3)$  nm and  $(9.1 \pm 1.9)$  nm (Figure 5d).

In the Ge–TaZrO<sub>x</sub> layers, which contain 36 at.% Ge and which are thicker than 6 nm, several Ge nuclei form at different vertical positions, because the wavelength of the composition modulations<sup>46,47</sup> is shorter than the composite layer thickness. However, as the wavelength of the composition modulations is not necessarily commensurable with the composite layer thickness, the Ge nanocrystals located at different vertical positions have different size and different volume, as seen in Figure 5. If the composite layers are much thicker than the wavelength of the composition modulations, the Ge nanocrystals show a single normal size distribution with a center. This expectation was confirmed by our previous experiments with 500-nm-thick Ge–TaZrO<sub>x</sub> composite layers, in which Ge nanocrystals with unimodal size distribution of about 4 nm are formed after annealing. The bigger sizes in the bimodal size distributions may be caused by the limited diffusion geometry in the superlattice structure.

In particular, in the Ge–TaZrO<sub>x</sub> composite layers, in which Ge nanocrystals having a multimodal size distribution are formed after annealing, Ostwald ripening is an important issue, because it can contribute to the growth of large Ge nanocrystals and to the disappearance of the small ones. Nevertheless, the above-mentioned results document that the size control of the Ge nanocrystals via adjustment of the Ge–TaZrO<sub>x</sub> layer thickness works reliably only up to a certain Ge–TaZrO<sub>x</sub> layer thickness, which is smaller than 9 nm for 36 at.% Ge.

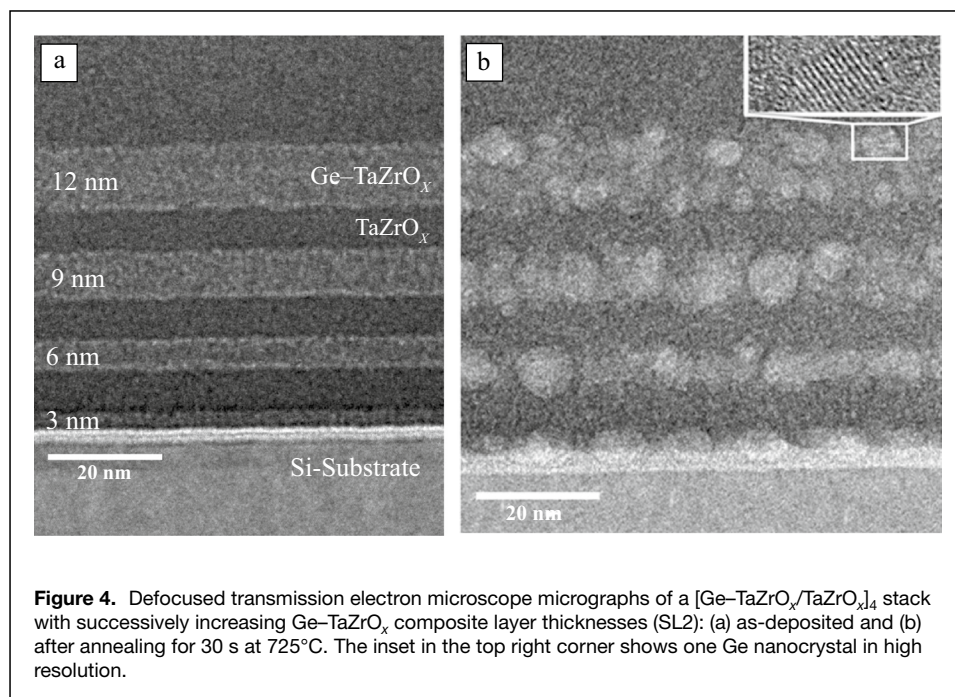


**Figure 4.** Defocused transmission electron microscope micrographs of a [Ge–TaZrO<sub>x</sub>/TaZrO<sub>x</sub>]<sub>4</sub> stack with successively increasing Ge–TaZrO<sub>x</sub> composite layer thicknesses (SL2): (a) as-deposited and (b) after annealing for 30 s at 725°C. The inset in the top right corner shows one Ge nanocrystal in high resolution.

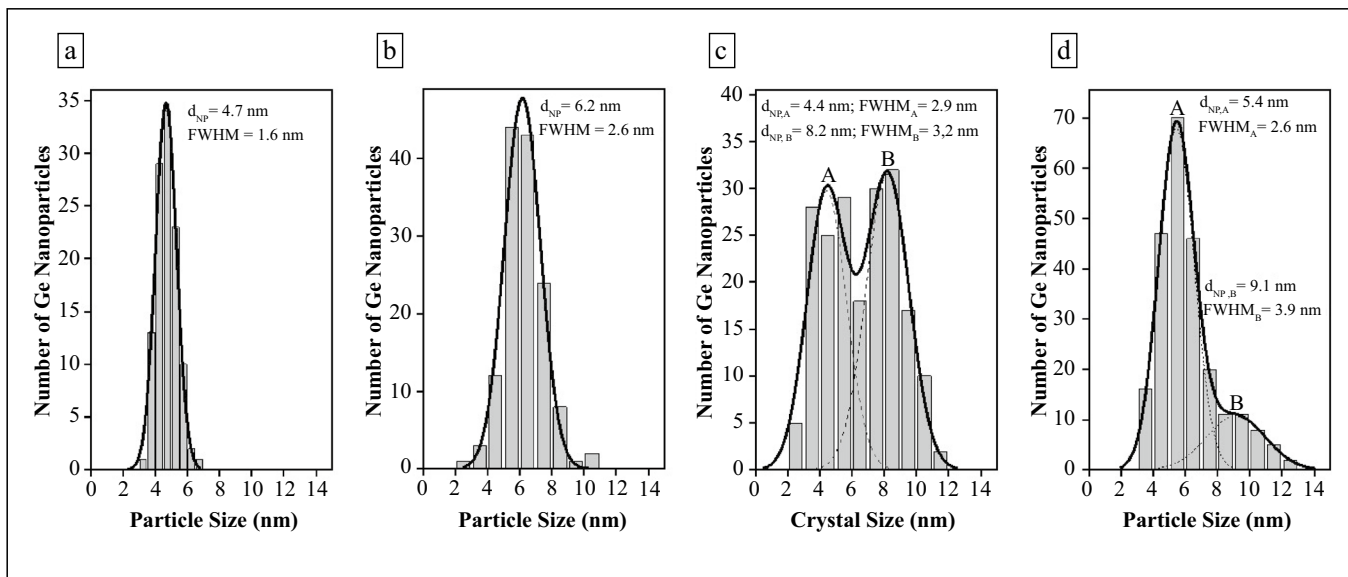


**Figure 5.** Size and size distribution of the Ge nanocrystals formed from Ge-TaZrO<sub>x</sub> composite layers of different thicknesses (SL2): (a) 3 nm, (b) 6 nm, (c) 9 nm, and (d) 12 nm after annealing at 725°C. The size distribution was fitted with one or two normal distributions. The center position ( $d_{NP}$ ) and the full width at half maximum (FWHM) are given in the respective figure.

### Effect of a SiO<sub>2</sub> layer underneath the GeTaZrO<sub>x</sub> composite layer on the growth of Ge nanocrystals [SL3]

The HRTEM micrograph of SL2 (Figure 4) suggests that Ge nanocrystals penetrate into the silicon dioxide, if they grow in contact with a SiO<sub>2</sub> layer. In order to elucidate the influence of

neighboring SiO<sub>2</sub> on the formation of Ge nanocrystals within the Ge-TaZrO<sub>x</sub> composite layers, the sample series SL3 was fabricated. In SL3, the composite layers have a Ge concentration of 36 at.% (the same as in SL2). However, SL3 uses additional SiO<sub>2</sub> layers, which are located beneath the Ge-TaZrO<sub>x</sub> composite layers. After annealing for 30 s at 725°C, two types

of Ge nanocrystals formed in SL3: larger nanocrystals with a direct contact to SiO<sub>2</sub> (Type I) and smaller nanocrystals without contact to SiO<sub>2</sub> (Type II). Even keeping in mind that TEM images in the defocus mode overestimate the nanocrystal size, we can state that the Type I nanocrystals appear to be better separated and more spherical shaped than the Type II nanocrystals.

The size and size distribution of nanocrystals in SL3 depends again strongly on the thickness of the composite layers (see Figures 6 and 7). In the first two layers having a thickness of 3 nm and 6 nm, the Ge nanocrystals have a unimodal size distribution. The mean diameter of the Ge nanocrystals is  $(6.3 \pm 2.6)$  nm and  $(9.4 \pm 3.3)$  nm for

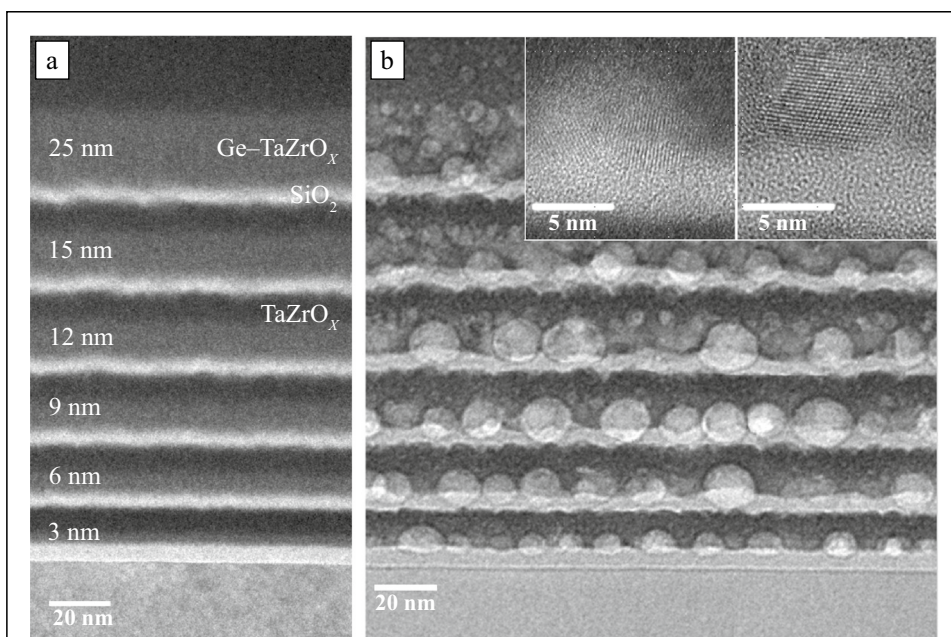


**Figure 6.** Defocused transmission electron microscope (TEM) micrographs of a [Ge-TaZrO<sub>x</sub>/SiO<sub>2</sub>/TaZrO<sub>x</sub>]<sub>6</sub> stack with successively increasing Ge-TaZrO<sub>x</sub> composite layer thicknesses and additional SiO<sub>2</sub> layers beneath the composite layers (SL3): (a) in the as-deposited state and (b) after annealing at 725°C. The insets in the top right corner show high-resolution TEM images without defocus affirming the crystallinity of the Ge clusters and the amorphous nature of the SiO<sub>2</sub> layers.

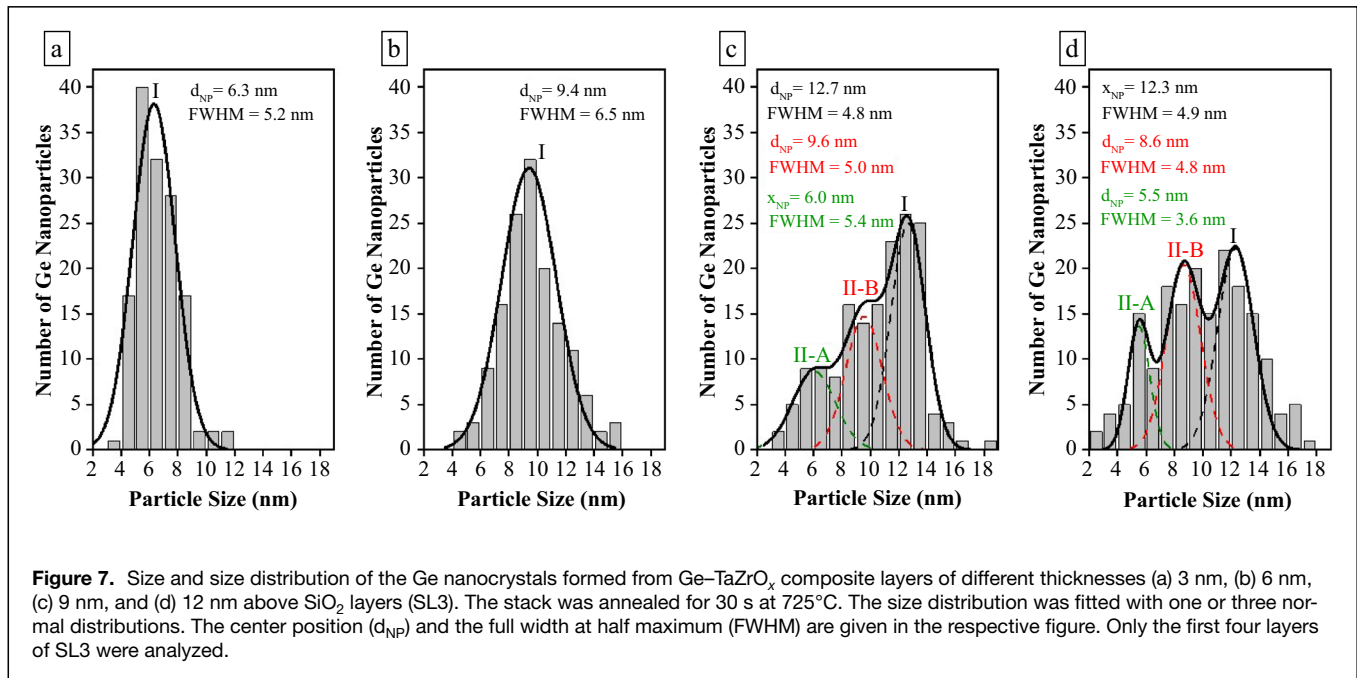


**Figure 7.** Size and size distribution of the Ge nanocrystals formed from Ge–TaZrO<sub>x</sub> composite layers of different thicknesses (a) 3 nm, (b) 6 nm, (c) 9 nm, and (d) 12 nm above SiO<sub>2</sub> layers (SL3). The stack was annealed for 30 s at 725°C. The size distribution was fitted with one or three normal distributions. The center position ( $d_{NP}$ ) and the full width at half maximum (FWHM) are given in the respective figure. Only the first four layers of SL3 were analyzed.

the initially 3- and 6-nm-thick composite layer, respectively. Hence, at the same composite layer thickness, the nanocrystals of the first two layers are significantly larger in SL3 than in SL2. In addition, the distribution of the crystallite size is much broader if the Ge nanocrystals grow on SiO<sub>2</sub> (SL3) than if they grow in the TaZrO<sub>x</sub> matrix (SL2). With increasing thickness of the Ge–TaZrO<sub>x</sub> layers, the size distribution of Ge nanocrystals becomes progressively larger. For the third and fourth layer having an initial thickness of 9 nm and 12 nm, respectively, the size distributions were approximated by three normal distribution functions. Besides the Type I nanocrystals, composite layers thicker than 6 nm contain several Type II nanocrystals at different vertical positions and with a bimodal size distribution like in SL2. This can again be explained with the wavelength of the composition modulations,<sup>46, 47</sup> which is shorter than the composite layer thickness.

It has been shown that there is no diffusion of Ge atoms into SiO<sub>2</sub> at 725°C.<sup>18</sup> Thus, we explain the growth of the Type I Ge nanocrystals into the SiO<sub>2</sub> layer (Figure 6) by a lower surface energy at the interface SiO<sub>2</sub>/Ge than at the Ge/TaZrO<sub>x</sub> interface, leading to a preferred nucleation process of the nanocrystals at the interface between the composite Ge/TaZrO<sub>x</sub> and the pure SiO<sub>2</sub> layer. The growing Ge nanocrystal displaces SiO<sub>2</sub>, which gives the impression of growth into the SiO<sub>2</sub> layer. However, this effect does not affect the spatial positioning significantly, due the stop of the growth at the underlying TaZrO<sub>x</sub>/SiO<sub>2</sub> interface. To prove this hypothesis, sample SL4 with Ge–SiO<sub>2</sub> composite layers was grown and investigated.

#### [TaZrO<sub>x</sub>/Ge–SiO<sub>2</sub>]<sub>n</sub> superlattice structure [SL4]

For comparison, the behavior of the mixed Ge–SiO<sub>2</sub> system in contrast to the Ge–TaZrO<sub>x</sub> material system was investigated on superlattice structure SL4. In this case, no penetration of the Ge nanocrystals into the TaZrO<sub>x</sub> separation layers can be detected by TEM imaging. This supports the assumption that the surface energy at the Ge/SiO<sub>2</sub> interface does not reinforce a crystal growth of the Ge clusters into the TaZrO<sub>x</sub> separation layers. The good barrier characteristics of the TaZrO<sub>x</sub> leads to a high positioning accuracy, as discussed earlier. However, the Ge segregation and hence the nanocrystal formation are much less developed than in the comparable Ge–TaZrO<sub>x</sub> layers for the same thermal budget (Figure 8a). A possible explanation of this phenomenon could be the mentioned smaller interface energy of Ge nanocrystals in SiO<sub>2</sub> compared to TaZrO<sub>x</sub> leading to a weaker driving force for Ge segregation. The formation of well-defined nanocrystals in an amorphous SiO<sub>2</sub> matrix may need a higher thermal budget (e.g., a deposition at increased temperatures).<sup>48</sup> An increase of the annealing temperature above 800°C, however, would lead to undesirable crystallization of the TaZrO<sub>x</sub> barrier layers.

#### Conclusions

Superlattices of Ge-containing composite layers and TaZrO<sub>x</sub> separation layers with the structures [Ge–TaZrO<sub>x</sub>/TaZrO<sub>x</sub>]<sub>n</sub>, [Ge–TaZrO<sub>x</sub>/SiO<sub>2</sub>/TaZrO<sub>x</sub>]<sub>6</sub>, and [TaZrO<sub>x</sub>/Ge–SiO<sub>2</sub>]<sub>n</sub> were

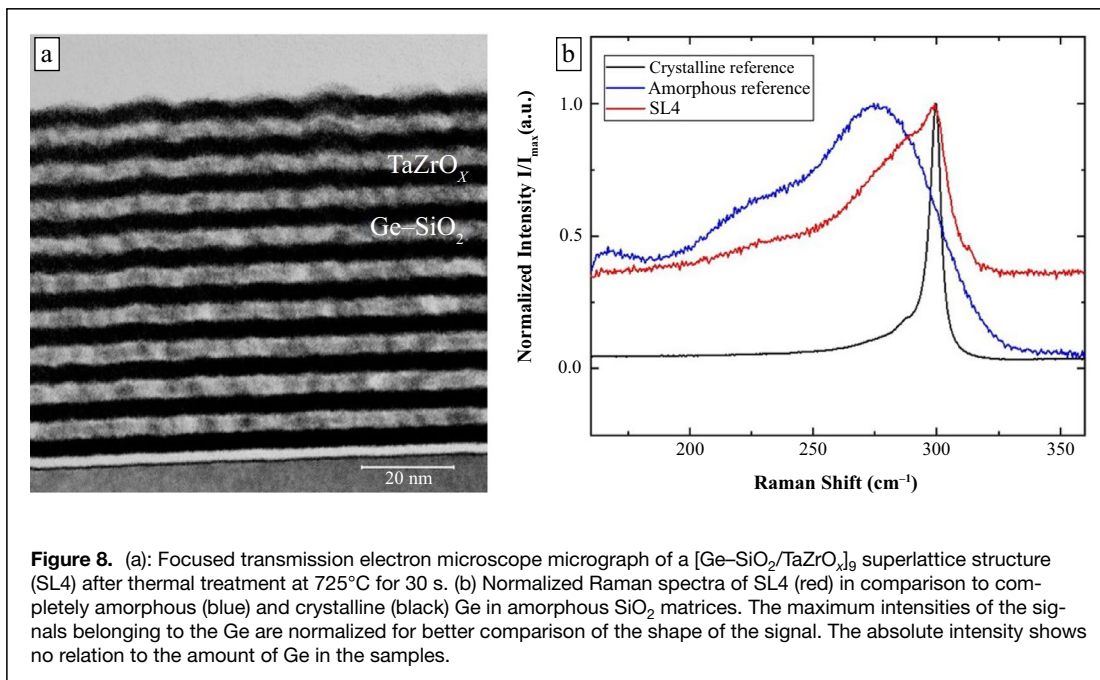


**Figure 8.** (a): Focused transmission electron microscope micrograph of a  $[\text{Ge-SiO}_2/\text{TaZrO}_x]_9$  superlattice structure (SL4) after thermal treatment at  $725^\circ\text{C}$  for 30 s. (b) Normalized Raman spectra of SL4 (red) in comparison to completely amorphous (blue) and crystalline (black) Ge in amorphous  $\text{SiO}_2$  matrices. The maximum intensities of the signals belonging to the Ge are normalized for better comparison of the shape of the signal. The absolute intensity shows no relation to the amount of Ge in the samples.

fabricated by confocal rf magnetron sputtering. Size-controlled crystalline Ge nanoclusters were successfully grown in an amorphous high- $k$  matrix by appropriate choice of matrix material and annealing procedure. By introducing  $\text{Ta}_2\text{O}_5$  into the  $\text{ZrO}_2$ , the amorphous phase of the matrix has been stabilized up to  $770^\circ\text{C}$ , whereas the Ge nanoclusters start to crystallize at  $700^\circ\text{C}$  for 30 s RTP annealing. Hence, the simultaneous crystallization of the Ge and the  $\text{ZrO}_2$ , which was reported several times for the system  $\text{Ge}/\text{ZrO}_2$ ,<sup>6, 24, 29</sup> has been successfully avoided. In this work, the superlattices deposited with an amorphous  $\text{TaZrO}_x$  matrix contain spherical shaped Ge nanocrystals with very good control over size and spatial distribution. This enables the use of this material system for applications such as nonvolatile memories. The formation of separated Ge nanoclusters can further be facilitated by increasing the Ge concentration in the  $\text{Ge-TaZrO}_x$  layers up to 50 at.%.

Nevertheless, there are minor drawbacks. Mainly, the nanocrystal size control is less efficient for mixed layers exceeding 6-nm thickness.  $\text{Ge-TaZrO}_x$  composite layers of 9 and 12 nm thickness form a bimodal nanocrystal size distribution, which is likely due to short-range composition modulations being smaller than the layer thickness. The lattice parameter of the Ge nanocrystals is found to deviate from the bulk value, which indicates the incorporation of foreign atoms (presumably Ta, Zr, O) and an incomplete phase separation into Ge and Ta and Zr based oxides. These impurities could influence the physical properties of the Ge nanocrystals.

The addition of a  $\text{SiO}_2$  layer underneath the composite layer ( $[\text{Ge-TaZrO}_x/\text{SiO}_2/\text{TaZrO}_x]_6$  superlattice stacks) leads to the formation of well-shaped and separated nanocrystals that penetrate into the  $\text{SiO}_2$  layer and in difference to  $\text{SiO}_2$ -free superlattices

to larger crystals. This is most likely due to the  $\text{Ge}/\text{SiO}_2$  interface, which is energetically favorable compared to the  $\text{Ge}/\text{TaZrO}_x$  interface. However, the distribution of the crystallite sizes is much broader here than for Ge nanocrystals grown in the  $\text{TaZrO}_x$  matrix only. At least the segregation

of Ge from the  $\text{Ge-TaZrO}_x$  composition layer leads to better results than the segregation from the  $\text{Ge-SiO}_2$  compound layer.

### Author contributions

Not applicable.

### Funding

Open Access funding enabled and organized by Projekt DEAL. For this work, no funding sources have to be acknowledged.

### Data availability

Raw data were generated at the institutions of the authors. Derived data supporting the findings of this study are available from the corresponding author upon request.

### Code availability

Not applicable.

### Conflict of interest

No conflicts of interest have to be declared.

### Open Access

This article is licensed under a Creative Commons Attribution 4.0 International License, which permits use, sharing, adaptation, distribution and reproduction in any medium or format, as long as you give appropriate credit to the original author(s) and the source, provide a link to the Creative Commons license, and indicate if changes were made. The images or other third party material in this article are included in the article's Creative Commons license, unless indicated otherwise in a credit line to the material. If material is not included



in the article's Creative Commons license and your intended use is not permitted by statutory regulation or exceeds the permitted use, you will need to obtain permission directly from the copyright holder. To view a copy of this license, visit <http://creativecommons.org/licenses/by/4.0/>.

## References

1. G. Conibeer, M. Green, R. Corkish, Y. Cho, E.-C. Cho, C.-W. Jiang, T. Fangsuwannarak, E. Pink, Y. Huang, T. Puzzer, T. Trupke, B. Richards, A. Shalav, K.-L. Lin, *Thin Solid Films* **511–512**, 654 (2006). <https://doi.org/10.1016/j.tsf.2005.12.119>
2. M. Fujii, M. Yoshida, S. Hayashi, K. Yamamoto, *J. Appl. Phys.* **84**(8), 4525 (1998). <https://doi.org/10.1063/1.368678>
3. V.Y. Timoshenko, M.G. Lisachenko, O. Shalygina, B.V. Kamenev, D.M. Zhigunov, S.A. Teterukov, P. Kashkarov, J. Heitmann, M. Schmidt, M. Zacharias, *J. Appl. Phys.* **96**(4), 2254 (2004). <https://doi.org/10.1063/1.1773383>
4. L. Pavesi, L.D. Negro, C. Mazzoleni, G. Franzò, F. Priolo, *Nature* **408**(6811), 440 (2000)
5. S. Tiwari, F. Rana, H. Hanafi, A. Hartstein, E.F. Crabbé, K. Chan, *Appl. Phys. Lett.* **68**(10), 1377 (1996). <https://doi.org/10.1063/1.116085>
6. D. Lehninger, P. Seidel, M. Geyer, F. Schneider, V. Klemm, D. Rafaja, J. von Borany, J. Heitmann, *Appl. Phys. Lett.* **106**(2), 23116 (2015). <https://doi.org/10.1063/1.4905933>
7. K.S. Min, K.V. Shcheglov, C.M. Yang, H.A. Atwater, M.L. Brongersma, A. Polman, *Appl. Phys. Lett.* **68**(18), 2511 (1996). <https://doi.org/10.1063/1.115838>
8. S. Cosentino, E.S. Ozen, R. Raciù, A.M. Mio, G. Nicotra, F. Simone, I. Crupi, R. Turan, A. Terrasi, A. Aydinli, S. Mirabella, *J. Appl. Phys.* **115**(4), 43103 (2014). <https://doi.org/10.1063/1.4863124>
9. L. Khomenkova, D. Lehninger, O. Kondratenko, S. Ponomaryov, O. Gudymenko, Z. Tsybrii, V. Yukhymchuk, V. Klado, J. von Borany, J. Heitmann, *Nanoscale Res. Lett.* **12**(1), 196 (2017). <https://doi.org/10.1186/s11671-017-1960-9>
10. P. Basa, G. Molnár, L. Dobos, B. Pécz, L. Tóth, A.L. Tóth, A.A. Koós, L. Dózsa, Á. Nemcsics, Zs. J. Horváth, *J. Nanosci. Nanotechnol.* **8**(2), 818 (2008). <https://doi.org/10.1166/jnn.2008.A122>
11. S. Takeoka, M. Fujii, S. Hayashi, K. Yamamoto, *Phys. Rev. B* **58**(12), 7921 (1998). <https://doi.org/10.1103/PhysRevB.58.7921>
12. U. Serincan, G. Kartopu, A. Guenes, T.G. Finstad, R. Turan, Y. Ekinci, S.C. Bayliss, *Semicond. Sci. Technol.* **19**(2), 247 (2004). <https://doi.org/10.1088/0268-1242/19/2/021>
13. J. Aldana, Y.A. Wang, X. Peng, *J. Am. Chem. Soc.* **123**(36), 8844 (2001). <https://doi.org/10.1021/ja016424q>
14. A. Dana, S. Ağan, S. Tokay, A. Aydinli, T.G. Finstad, *Phys. Status Solidi C* **4**(2), 288 (2007). <https://doi.org/10.1002/pssc.200673233>
15. S. Foss, T.G. Finstad, A. Dana, A. Aydinli, *Thin Solid Films* **515**(16), 6381 (2007). <https://doi.org/10.1016/j.tsf.2006.11.094>
16. M. Zacharias, J. Bläsing, P. Veit, L. Tsybeskov, K. Hirschman, P.M. Fauchet, *Appl. Phys. Lett.* **74**(18), 2614 (1999). <https://doi.org/10.1063/1.123914>
17. F. Gourbilleau, X. Portier, C. TERNON, P. Voivenel, R. Madelon, R. Rizk, *Appl. Phys. Lett.* **78**(20), 3058 (2001). <https://doi.org/10.1063/1.1371794>
18. M. Zschintzsch, N.M. Jeutter, J. von Borany, M. Krause, A. Mücklich, *J. Appl. Phys.* **107**(3), 34306 (2010). <https://doi.org/10.1063/1.3276184>
19. D. Lehninger, J. Beyer, J. Heitmann, *Phys. Status Solidi A* **155**, 1701028 (2018). <https://doi.org/10.1002/pssa.201701028>
20. J.D. Budai, C.W. White, S.P. Withrow, M.F. Chisholm, J. Zhu, R.A. Zuhr, *Nature* **390**(6658), 384 (1997). <https://doi.org/10.1038/37079>
21. I.D. Sharp, Q. Xu, D.O. Yi, C.W. Yuan, J.W. Beeman, K.M. Yu, J.W. Ager III, D.C. Chrzan, E.E. Haller, *J. Appl. Phys.* **100**(11), 114317 (2006). <https://doi.org/10.1063/1.2398727>
22. C. Schubert, U. Kaiser, A. Hedler, W. Wesch, T. Gorelik, U. Glatzel, J. Kräußlich, B. Wunderlich, G. Heß, K. Goetz, *J. Appl. Phys.* **91**(3), 1520 (2002). <https://doi.org/10.1063/1.1430539>
23. V.A. Volodin, E.B. Gorokhov, M.D. Efremov, D.V. Marin, D.A. Orekhov, *JETP Lett.* **77**(8), 411 (2003). <https://doi.org/10.1134/1.1587174>
24. S. Haas, F. Schneider, C. Hincinschi, V. Klemm, G. Schreiber, J. von Borany, J. Heitmann, *J. Appl. Phys.* **113**, 044303 (2013). <https://doi.org/10.1063/1.4780033>
25. J. Robertson, *J. Vac. Sci. Technol. B* **18**(3), 1785 (2000). <https://doi.org/10.1116/1.591472>
26. D. Panda, T.-Y. Tseng, *Thin Solid Films* **531**, 1 (2013). <https://doi.org/10.1016/j.tsf.2013.01.004>
27. X. Zhao, D. Vanderbilt, *Phys. Rev. B* (2002). <https://doi.org/10.1103/PhysRevB.65.075105>
28. P. Seidel, M. Geyer, D. Lehninger, F. Schneider, V. Klemm, J. Heitmann, *ECS Trans.* **53**(1), 237 (2013). <https://doi.org/10.1149/05301.0237ecst>
29. D. Lehninger, L. Khomenkova, C. Röder, G. Gärtner, B. Abdenroth, J. Beyer, F. Schneider, D.C. Meyer, J. Heitmann, *ECS Trans.* **66**(4), 203 (2015). <https://doi.org/10.1149/06604.0203ecst>
30. E. Agocs, Z. Zolnai, A.K. Rossall, J.A. van den Berg, B. Fodor, D. Lehninger, L. Khomenkova, S. Ponomaryov, O. Gudymenko, V. Yukhymchuk, B. Kalas, J. Heitmann, P. Petrik, *Appl. Surf. Sci.* **421**, 283(2017). <https://doi.org/10.1016/j.apsusc.2017.03.153>
31. T.-W. Kim, C.-H. Cho, B.-H. Kim, S.-J. Park, *Appl. Phys. Lett.* **88**(12), 123102 (2006). <https://doi.org/10.1063/1.2187434>
32. A. Krause, W.M. Weber, U. Schröder, D. Pohl, B. Rellinghaus, J. Heitmann, T. Mikolajick, *Appl. Phys. Lett.* **99**, 222905 (2011). <https://doi.org/10.1063/1.3664395>
33. D. Lehninger, D. Rafaja, J. Wünsche, F. Schneider, J. von Borany, J. Heitmann, *Appl. Phys. Lett.* **110**(26), 262903 (2017). <https://doi.org/10.1063/1.4990529>
34. M. Ferrari, L. Lutterotti, S. Matthies, P. Polonioli, H.R. Wenk, *Mater. Sci. Forum* **228–231**, 83 (1996). <https://doi.org/10.4028/www.scientific.net/MSF.228-231.83>
35. L. Lutterotti, S. Matthies, H.-R. Wenk, *ICOTOM-12* **21**, 14 (1999)
36. Z. Iqbal, S. Veprek, *J. Phys. C* **15**(2), 377 (1982). <https://doi.org/10.1088/0022-3719/15/2/019>
37. H. Fukuda, T. Kobayashi, T. Endoh, S. Nomura, A. Sakai, Y. Ueda, *Appl. Surf. Sci.* **130–132**, 776 (1998). [https://doi.org/10.1016/S0169-4332\(98\)00153-6](https://doi.org/10.1016/S0169-4332(98)00153-6)
38. A.S. Cooper, *Acta Crystallogr.* **15**(6), 578 (1962). <https://doi.org/10.1107/S0365110X62001474>
39. K. Lehovc, *J. Less-Common Met.* **7**(6), 397 (1964). [https://doi.org/10.1016/0022-5088\(64\)90036-0](https://doi.org/10.1016/0022-5088(64)90036-0)
40. E.H. Kisi, C.J. Howard, R.J. Hill, *J. Am. Ceram. Soc.* **72**(9), 1757 (1989). <https://doi.org/10.1111/j.1151-2916.1989.tb06322.x>
41. G.K. Williamson, W.H. Hall, *Acta Metall.* **1**(1), 22 (1953)
42. D. Rafaja, H. Fuess, D. Šimek, L. Zdeborová, V. Valvoda, *J. Phys.* **14**(43), 10021 (2002). <https://doi.org/10.1088/0953-8984/14/43/301>
43. S.P. Garg, N. Krishnamurthy, M. Venkatraman, S. Raju, *J. Phase Equilib.* **12**(6), 661 (1991). <https://doi.org/10.1007/BF02645166>
44. W. Kaiser, C.D. Thurmond, *J. Appl. Phys.* **32**(1), 115 (1961). <https://doi.org/10.1063/1.1735936>
45. A. Chronopoulos, A. Dimoulas, *J. Appl. Phys.* **111**(2), 23714 (2012). <https://doi.org/10.1063/1.3679089>
46. J.W. Cahn, *Acta Metall.* **9**(9), 795 (1961). [https://doi.org/10.1016/0001-6160\(61\)90182-1](https://doi.org/10.1016/0001-6160(61)90182-1)
47. J.W. Cahn, *J. Chem. Phys.* **42**(1), 93 (1965). <https://doi.org/10.1063/1.1695731>
48. B. Zhang, S. Shrestha, M.A. Green, G. Conibeer, *Appl. Phys. Lett.* **96**(26), 261901 (2010). <https://doi.org/10.1063/1.3457864> □